Inertial focusing in triangular microchannels with various apex angles

Cite as: Biomicrofluidics **14**, 024105 (2020); https://doi.org/10.1063/1.5133640
Submitted: 25 October 2019 . Accepted: 11 March 2020 . Published Online: 24 March 2020

Jeong-ah Kim, Aditya Kommajosula, Yo-han Choi, Je-Ryung Lee, Eun-chae Jeon, Baskar Ganapathysubramanian, and Wonhee Lee

Biomicrofluidics ARTICLE scitation.org/journal/bmf

Inertial focusing in triangular microchannels with various apex angles

Cite as: Biomicrofluidics 14, 024105 (2020); doi: 10.1063/1.5133640
Submitted: 25 October 2019 · Accepted: 11 March 2020 ·
Published Online: 24 March 2020

View Online Export Citation CrossMark

Jeong-ah Kim,[1] Aditya Kommajosula,[2] Yo-han Choi,[3] Je-Ryung Lee,[4] Eun-chae Jeon,[5] Baskar Ganapathysubramanian,[2,a)] and Wonhee Lee[1,3,6,a)]

AFFILIATIONS

[1]Department of Physics, Korea Advanced Institute of Science and Technology (KAIST), Daejeon 34141, South Korea
[2]Department of Mechanical Engineering, Iowa State University (ISU), Ames, Iowa 50011, USA
[3]Graduate School of Nanoscience and Technology, KAIST, Daejeon 34141, South Korea
[4]Department of Electronics and Information Engineering, Korea University, Sejong 30019, South Korea
[5]School of Materials Science & Engineering, University of Ulsan, Ulsan 44610, South Korea
[6]Department of Bio and Brain Engineering, KAIST, Daejeon 34141, South Korea

[a)]**Authors to whom correspondence should be addressed:** baskarg@iastate.edu and whlee153@kaist.ac.kr

ABSTRACT

We consider inertial focusing of particles in channels with triangular cross sections. The number and the location of inertial focusing positions in isosceles triangular channels can change with varying blockage ratios (a/H) and Reynolds numbers (Re). In triangular channels, asymmetric velocity gradient induced by the sloped sidewalls leads to changes in the direction and the strength of the inertial lift forces. Therefore, varying the configuration (specifically, angle) of the triangular cross section is expected to lead to a better understanding of the nature of the inertial lift forces. We fabricated triangular microchannels with various apex angles using channel molds that were shaped by a planing process, which provides precise apex angles and sharp corners. The focusing position shift was found to be affected by the channel cross section, as expected. It was determined that the direction of the focusing position shift can be reversed depending on whether the vertex is acute or obtuse. More interestingly, corner focusing modes and splitting of the corner focusing were observed with increasing Re, which could explain the origin of the inertial focusing position changes in triangular channels. We conducted fluid dynamic simulations to create force maps under various conditions. These force maps were analyzed to identify the basins of attraction of various attractors and pinpoint focusing locations using linear stability analysis. Calculating the relative sizes of the basins of attractions and exhaustively identifying the focusing positions, which are very difficult to investigate experimentally, provided us a better understanding of trends in the focusing mechanism.

INTRODUCTION

Studies of inertial microfluidics have received growing attention in the past decade as the importance of fluid inertia in the physics of microfluidics has been recognized.[1–6] Many interesting inertial effects have been discovered with microfluidic flows at a Reynolds number of $\sim 1 < Re < \sim 100$. Within such flows, particles are observed to migrate and focus into distinct equilibrium positions; this is called inertial focusing. Numerous studies have revealed the underlying physical mechanism of inertial focusing since its original discovery in 1961.[7] Our current understanding is that it is based on the balance of two major inertial lift forces: the shear-gradient lift force and wall-effect lift force.[8] The magnitude of the lift forces depends on the size of the particle relative to the channel dimension. Particularly, for microfluidic channels, the size of the microparticles or cells is large enough; hence, the magnitude of the inertial lift forces becomes highly efficient for manipulating microparticles or cells.[9] This behavior can be exploited for applications in diverse areas.[10–13]

The locations of the inertial focusing position depend on various parameters, including Re,[14] particle size,[9] particle shape,[15] and the cross-sectional shape of the channel.[16] Inertial focusing within microchannels with a rectangular cross section has been

extensively studied.[9,17] In rectangular channels, the changes in inertial focusing positions induced by the aforementioned parameters are relatively small. One exceptional case is the change with the channel aspect ratio; four focusing positions in square channels change to two focusing positions in rectangular channels with high aspect ratios.[17–19] Using these dramatic changes in focusing positions, it was shown that highly efficient particle separation[20] and fluid exchange processes were feasible.[17,21] As these examples illustrated, altering the focusing positions allows novel and efficient methods such as single cell analysis and cell separation for various applications. Various methods to manipulate focusing positions have been developed to realize these. In particular, the use of secondary flows to shift inertial focusing positions has been extensively studied. For example, spiral,[22] serpentine,[23] and expansion–contraction channels[24] can be used for highly efficient cell separations because the differences in inertial focusing positions for different sized particles can be amplified in these systems. The use of additional forces, including viscoelastic, acoustic, and magnetic forces, is among the approaches suitable for altering inertial focusing positions.[25–28]

The shape of the channel cross section has also been recently recognized as a convenient parameter for altering inertial focusing positions as suggested by various fabrication methods.[29–31] Studies of inertial focusing in microchannels with non-rectangular cross sections have suggested that varying the channel cross section shape allows control of the magnitudes and directions of the inertial lift forces, thereby providing powerful ways to alter the inertial focusing positions.[16,30–34] For example, the sloped sidewalls and ensuing (top–bottom) asymmetric velocity gradient of a triangular channel lead to variations in the direction and the strength of the inertial lift forces. As a result, many interesting variations of the inertial focusing positions have been found in triangular channels, which led to applications in various fields.[16,31–34] Inertial focusing in channels with an equilateral right triangular cross section has been thoroughly investigated, with varying *Re* and particle size. Normally in triangular channels, particles are focused at the top and bottom focusing positions. However, the top focusing positions(s), which are influenced by the wall-effect lift forces of the two adjacent sidewalls, have shown large variations depending on *Re* and particle size. While relatively small particles are focused at the two *face focusing positions* near the faces of the sidewalls, relatively large particles are focused at a single *corner focusing position* near the apex. The top corner focusing position for relatively larger particles may also split into two side focusing positions, and shift away from the apex along the sidewalls, with increasing *Re*. The onset *Re* of the splitting is strongly dependent on the particle size, which can lead to highly efficient size-based microparticle separation.

The splitting and shifting of the top focusing position in triangular channels are believed to be determined by the balance of the shear-gradient lift force and the wall-effect lift forces from the sidewalls. It is expected that the directions and magnitude of the inertial lift forces can be readily controlled by the angles of the triangular channels. In this study, we numerically and experimentally investigated inertial focusing in triangular channels with various apex angles (45°, 60°, 90°, and 120°). The alteration of basins of attractions and changes in the corresponding focusing positions with varying *Re* and particle size was observed, revealing that inertial focusing positions are strongly dependent on the apex angles.

EXPERIMENTAL

Fabrication of triangular channel

A planing process was used to fabricate the channel molds from a bulk metal piece (Fig. S1 in the supplementary material). Workpieces made of brass were scraped with diamond cutting tools with a V-shaped edge and a specific angle. The angles of the triangular grooves on the workpiece were determined by the diamond cutting tools. The size, or depth, of the grooves is easily controlled by adjusting the cutting depth. In a previous study, we fabricated triangular channels with isosceles right triangle cross sections, using the planing process.[32] Furthermore, we showed that microchannels could be produced not only with exact angles but also with clean surfaces and sharp corners, and they are generally superior to the channels fabricated by other methods.[29,33,35,36] In the present research, we fabricated triangular channels with 45°, 60°, and 120° apex angles and various depths (Fig. 1). After the brass master molds were made with the planing processes, PDMS (Polydimethylsiloxane) replica molds were fabricated by conventional soft lithography techniques and used to make the PDMS channels.

Experimental setup and measurement

Although the difference in density between the particle and fluid is known to have little effect on inertial focusing, the densities of the fluid and microparticles were matched as a precaution to observe the motion of neutrally buoyant particles. NaCl was added to the particle suspension to match the fluid density to 1.03 g/cm^3, which is the density of the polystyrene particles (Micromer). In addition, Tween 20 [1% (v/v), Sigma-Aldrich] was added to prevent particle aggregation. We used low particle concentration for the particles focus at additional focusing positions formed by particle–particle interactions at high volume fraction.[37,38] The volume fraction was 4.9×10^{-4} for 10 μm, 1.6×10^{-3} for 15 μm, and 3.9×10^{-3} for 20 μm diameter particles.

We investigated inertial focusing in a wide range of conditions by changing the angle, Reynolds number, and blockage ratio (k). Table S1 in the supplementary material summarizes the conditions for the experiments and the numerical simulations. The particle

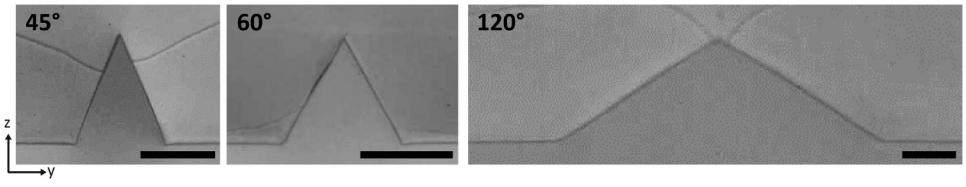

FIG. 1. The cross-sectional images of PDMS channels replicated from metallic molds that were machined by the planing process (scale bar 50 μm).

suspension was injected while controlling the volumetric flow rate with a syringe pump (Harvard Apparatus, PHD ULTRA CP syringe pump). By adjusting the volumetric flow rate, we changed *Re* from 20 to 140 in 20 intervals. *Re* was defined as $\mathrm{Re} = \frac{\rho UH}{\mu}$, where H is the hydraulic diameter, ρ and μ are the density and dynamic viscosity of the fluid, respectively, and U is the average velocity of the fluid. We observed particle dynamics from top and side views of the channel near the outlet using an optical microscope (Nikon Eclipse Ti-U) equipped with a high-speed camera (Phantom v7.3). Inertial focusing in triangular channels needs ~2 cm for efficient focusing with $Re = 15$–100.[39] We used the various triangular channels with a length of 3.5 cm, and the observation of focusing position was conducted near the outlet of the channels. We defined the coordinate system as follows: x axis in the flow direction, y axis in the width (w) direction, and z axis in the height (h) direction (Fig. S2 in the supplementary material). We confirmed that the blockage ratio k ($k = a/H$, a = particle diameter and H = hydraulic diameter) resulted in the same nondimensional focusing positions in the cross section (y/w, z/h) in a previous study.[32] Again, to confirm that k would be a fairly good representative parameter for inertial focusing in triangular channels, various k values were tested with various combinations of particle sizes and microchannel dimensions. No significant differences in focusing positions were found for the same k conditions.

Numerical simulation

We use the approach of "constrained simulations" to construct cross-sectional force maps of the particle lifts. This approach has been widely used in inertial migration studies to examine focusing points from cross-sectional force maps of the lifts.[9] This allows us to employ a steady-state fluid–structure interaction-based solver since we are not interested in the transient behavior of the particle. Rather our focus here is to find locations in the cross section where the particle streamwise drag and net torque = 0. For any given channel shape, *Re*, and k, we sampled the cross section for various particle locations, where we calculate lift forces on the particle by numerically integrating the fluid stresses on the particle. At each particle location, we solved the Navier–Stokes equations for fluid velocity and pressure along with particle streamwise velocity u_p and angular velocity ω_p by requiring that the streamwise drag and torque on the particle should vanish. The remaining force components, namely, the cross-sectional lifts, were computed at these particle velocities and indicated the tendency of the particle to equilibrate. This process was repeated for all of the sampled locations, and the net forces on the particles at these locations were collectively obtained as a force map. As detailed in our previous work,[40] we checked for the equilibrium points (zeros) of these forces. Once an equilibrium point was found, we represented the particle motion around that point as a 4×4 linearized dynamical system in terms of the net lifts in both directions (y and z). The nature of the equilibrium point was found by inspecting the eigenvalues of the stability matrix of this system. All negative real parts indicated that it was a stable point, while even one positive real part meant that it was an unstable point and, hence, not a focusing location.

We used a finite element code based on a stabilized formulation of the 3D stationary, incompressible, Navier–Stokes equations, namely, the Streamline Upwind Petrov–Galerkin/Pressure Stabilized Petrov–Galerkin (SUPG/PSPG) method.[41] The equations are solved on a boundary-fitted mesh, and the simulations are performed in an inertial translating reference frame attached to the particle (moving at the equilibrium streamwise velocity, u_p). No-slip conditions are imposed on the particle surface. The walls are set to translate backward (at a velocity, $-u_p$), and fully developed velocities ($-u_p$) are imposed at the inlet and outlet (the inlet and outlet are sufficiently distant from the particle). The particle was allowed to rotate at an angular velocity, ω_p. The net forces on the particle are evaluated as a surface integral of the pressure and viscous forces, which takes into account all force components present in inertial flows (such as shear-gradient lift, wall lift, etc.). The following equation is used to compute net forces (F represents forces, P is the pressure, u is the velocity, $\hat{n}$ is the surface normal, and Γ is the particle surface):

$$\boldsymbol{F} = \int_{\Gamma} \left(-P\bar{\bar{I}} + \frac{1}{Re}(\nabla \boldsymbol{u} + \nabla^T \boldsymbol{u}) \right) \cdot \hat{\boldsymbol{n}} d\Gamma.$$

RESULTS

Inertial focusing in 60° triangular channels

First, we investigated inertial focusing in 60° triangular channels. The 60° triangular channels have the highest degree of symmetry among all triangular channels. We experimentally and numerically investigated changes in the inertial focusing positions with $k = 0.27$ [Figs. 2(a) and 2(c)] and 0.43 [Figs. 2(b) and 2(d)]. The specific experimental conditions were as follows: for $k = 0.27$, (a, w, h) = (10 μm, 65 μm, 56 μm) and for $k = 0.43$, (a, w, h) = (15 μm, 60 μm, 52 μm). The particle positions from the top view and the side view of the channel were measured 3.5 cm downstream from the inlet. Figures 2(a) and 2(b) show the normalized statistical distributions of the measured particle positions. The particle count, n, was 1000, and the bin size was 1 μm. P represents the normalized count.

Multiple peaks were prominently observed in the statistics, representing the inertial focusing positions. The peak positions are plotted as a function of *Re* in Figs. 2(c) and 2(d). The error bars represent the standard deviations of the particle positions within each peak. Representative high-speed capture images of the particles are shown for each focusing position. For $k = 0.27$ [Figs. 2(a) and 2(c)], the distribution of particle positions shows three peaks in the top view and two peaks in the side view over the entire *Re* conditions. This indicates three inertial focusing positions near the center of each sidewall. Moreover, all of the peaks locations are almost identical for all *Re* conditions. This result confirms that the inertial focusing positions do not shift along the sidewalls in the 60° triangular channel. For $k = 0.43$, the particle position data look similar to the case of $k = 0.27$, except when $Re = 20$ [Figs. 2(b) and 2(d)]. At $Re = 20$, two additional peaks near $y/w = \pm 0.18$ were observed in the top view and another peak near $z/h = 0.58$ was observed in the side view. In the high-speed capture images, particles are shown at different focusing positions. The images of the particles look different when they are at different z-height. Interestingly, two different groups of images were observed for the particles focused near

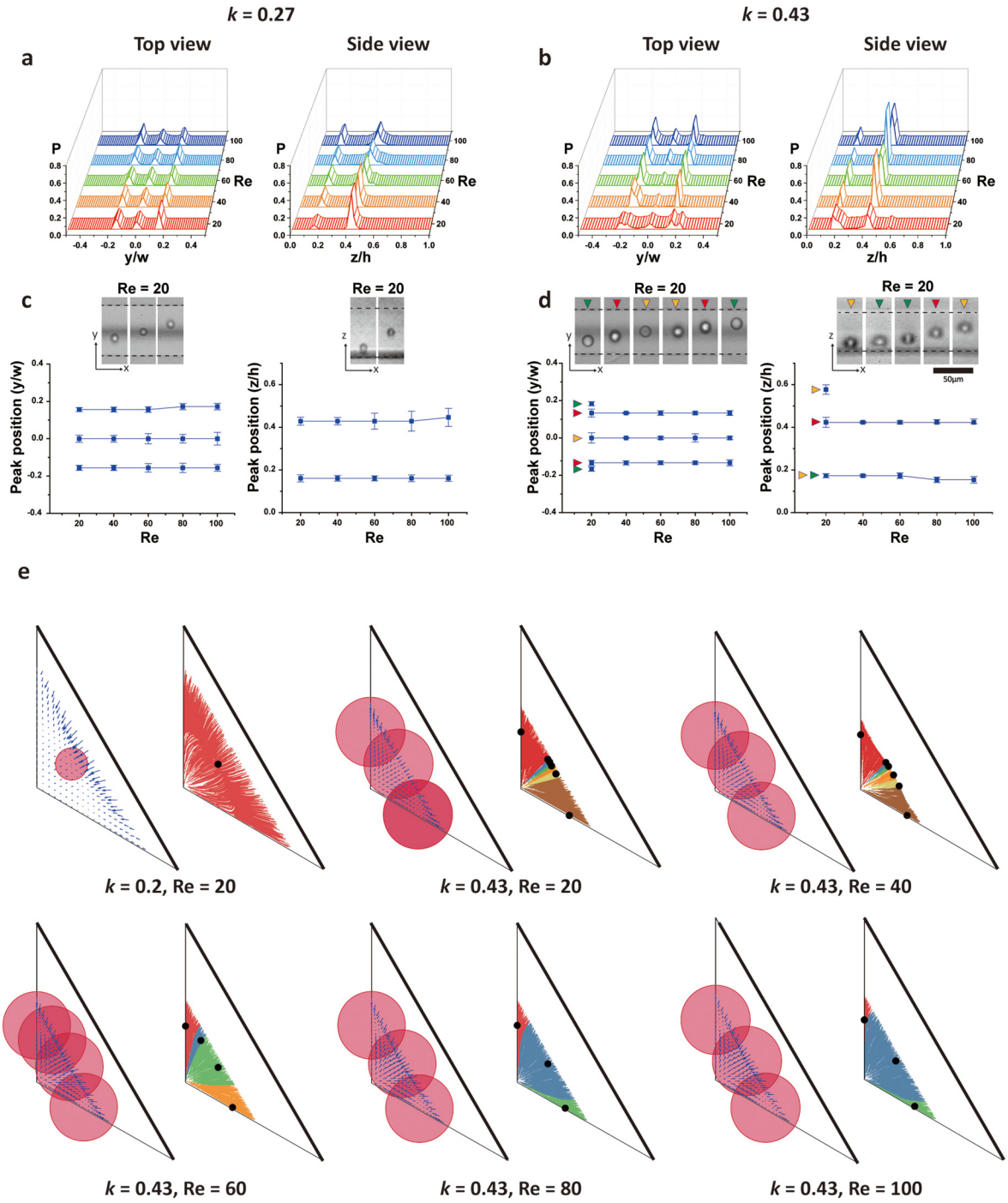

FIG. 2. Inertial focusing in 60° triangular channels with varying *Re* at $k = 0.27$ and $k = 0.43$. (a) and (b) The statistics of the particle positions ($n = 1000$) measured from the top view and side view. (c) and (d) The change in peak positions (i.e., focusing position) with varying *Re* obtained from (a) and (b). The high-speed images show the particles located at corresponding peak positions. (e) The numerical simulation of the lift forces in one third of the cross section (due to symmetry considerations) for conditions of ($k = 0.27$, $Re = 20$) and ($k = 0.43$, $Re = 20$, 40, 60, 80, 100). Red circles and black dots indicate the inertial focusing positions. Red circles are drawn as a scale of particle size, and black dots represent the pinpoint focusing locations. The individual basin of attraction that leads to each focusing position is shown in different colors on the right: green for top corner, red for top face, brown for bottom corner, and pink/orange/yellow for miscellaneous points.

$y/w = 0$. Side view images also suggest that there were more than one focusing positions along the bottom wall. The confocal microscopy images also support the analysis of the high-speed images (Fig. S3a in the supplementary material).

These observations suggest that there are stable focusing positions at each channel face and corner. We designated the focusing positions near the vertices of the triangle "corner focusing" and focusing positions near the center of the faces of the triangle "face focusing." The detailed name of focusing positions was described in Fig. S4 in the supplementary material. At $Re = 20$ for large k, the peaks in the statistics of the particle position suggested three corner focusing positions near every vertex in addition to the three face focusing positions. The corner focusing peaks disappeared and only the peaks for face focusing could be observed when $Re > 40$. Furthermore, no shift in peaks was observed.

The experimental results were confirmed by numerical simulations [Fig. 2(e)]. The numerical simulations were conducted for 1/3 of the entire cross section [Fig. 2(e)] due to 120° rotational symmetry. The force map allows us to divide the cross section into several basins of attraction, which contain one focusing position. The area of basins of attraction is closely related to the probability that particles will be found at the corresponding focusing position. In fact, some of the stable equilibrium positions in the force map did not appear as focusing positions in the experimental results. This is possibly if little particles are initially released in that particular basin of attraction with small area.

For $k = 0.27$, only three face focusing positions were found in the simulation results, regardless of Re, which agreed with the experimental results. The force map for $Re = 20$ and $k = 0.27$ is shown in Fig. 2(e). In contrast, the transition from dominant corner focusing to dominant face focusing was observed for $k = 0.43$ across $Re = 20$–100. Stable equilibrium positions were found at the locations that corresponded to all three corner focusing positions and three face focusing positions at $Re = 20$. In the meanwhile, the area of the basins of attraction changed with Re. The basins of attraction corresponding to corner focusing became narrower with increasing Re, while the basins of attraction for face focusing became larger [Fig. 2(e)]. For instance, corner focusing was still observed at $Re = 100$ for $k = 0.43$ even though the corresponding basins of attraction were negligibly small. Note that the possibility of finding particles at a focusing position is also dependent on the volumetric flow rate within the corresponding basin of attraction. In other words, a basin of attraction occupying the area near a corner would attract relatively fewer particles to the corresponding focusing position, which could explain why the corner focusing was only observed at $Re = 20$ in the experimental results.

The face focusing positions, interestingly, appeared as clouds of focusing positions at relatively low Re ($Re = 20$ and 40). Considering that the distances between the individual focusing positions are fairly small compared to the particle size, the cloud of focusing positions may be seen as a single broad peak in the experiment. However, the side view peak for the face focusing at $Re = 40$ was as sharp as the peaks at $Re > 40$, suggesting some discrepancy between simulation and experimental results over Re where the transition occurs. The cloud of focusing positions became a single focusing position with a larger basin of attraction as Re increased. In the experiment, merging of the face focusing position seemed to occur at a lower Re than in the simulation.

Inertial focusing in 45° triangular channels

We experimentally and numerically investigated inertial focusing with $k = 0.24$ and 0.45 while varying Re. A planing process enabled us to fabricate triangular channels with sharp corners, which provided proper experiment conditions even for an apex angle of 45°. The specific experimental conditions were as follows: for $k = 0.24$, $(a, w, h) = (10\,\mu\text{m}, 61\,\mu\text{m}, 74\,\mu\text{m})$ and for $k = 0.45$, $(a, w, h) = (15\,\mu\text{m}, 50\,\mu\text{m}, 61\,\mu\text{m})$. For $k = 0.24$, the statistics of the particle positions showed three peaks in the top view and two peaks in the side view over the entire Re range, which indicated three face focusing positions [Fig. 3(a)]. These focusing positions could also be confirmed from confocal microscopy (Fig. S3b, left in the supplementary material). The peak positions are plotted as a function of Re in Fig. 3(c). At $Re = 20$, the peak for the bottom focusing position is hardly distinguishable in the top view, while it is relatively sharp in the side view. We have identified the broad peaks with red color to distinguish them from other peaks that could be identified clearly ($P = 0.01$~0.03 red, $P > 0.03$ blue). The peak positions in the top view barely changed with Re; however, the peak positions corresponding to the top face focusing shifted slightly toward the apex in the side view with increasing Re. For $k = 0.45$ [Fig. 3(b)], only two side peaks can be observed in the top view and one peak can be observed in the side view at relatively low Re, which correspond to top face focusing positions. It was also confirmed from confocal microscopy that only two top face focusing positions were occupied in a large k and low Re condition (Fig. S3b, right in the supplementary material). The middle peak that corresponds to bottom face focusing becomes identifiable when $Re \geq 80$ in the top view and $Re \geq 60$ in the side view. Figure S5 in the supplementary material shows the enlarged particle distribution for the peak for the bottom face focusing in the side view. These results indicate that two face focusing positions near sidewalls are stable, while the unstable bottom focusing positions become stable at high Re. A similar trend is known for high-aspect-ratio rectangular channels.[1,42] The peak shift for the top focusing position is larger than $k = 0.24$, and its direction is toward the apex with increasing Re [Fig. 3(d)].

In the side view data for $Re = 20$ with $k = 0.45$, an extra peak was found at an unexpected position, $z/h \sim 0.42$. We analyzed the data further in detail from individual capture images. Interestingly, the particles found at this point only appear as pairs, with particles focused at the top face focusing position on opposite sides (see Fig. S6 in the supplementary material). We used fairly low particle concentration to minimize the focusing position developed by the particle–particle interaction. However, the speed of particle differs at the different cross-sectional positions, and self-assembled pairs of particles can be found with a relatively large probability.[42] We checked the location of these additional peaks in the cross section (Fig. S6c in the supplementary material). The positions did not match with any focusing positions observed in the other conditions. Inter-particle interactions and the wall-particle interaction are known to cause the self-assembly of inertially focused particles.[35] We believe that the additional inertial focusing positions were stabilized by

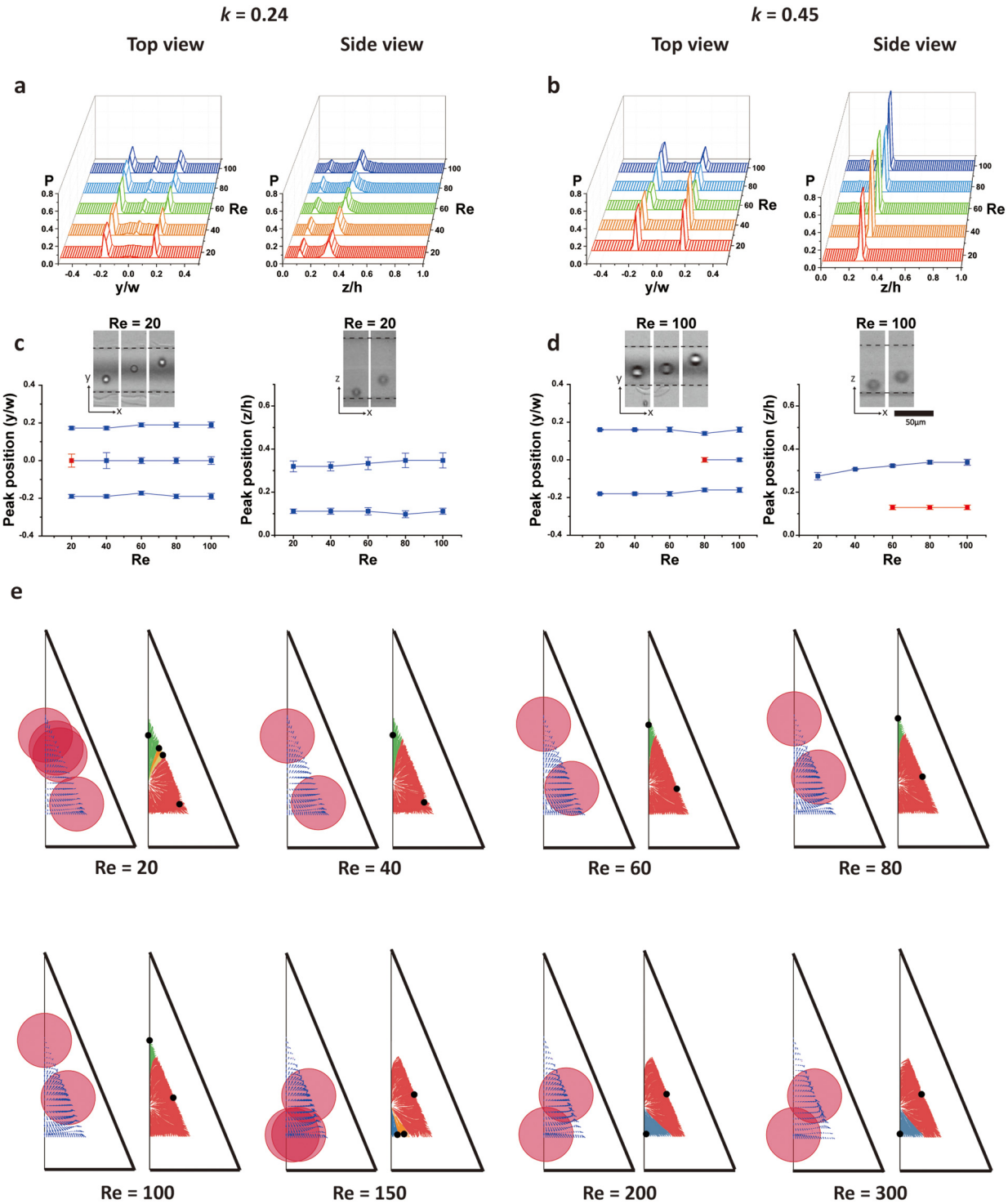

FIG. 3. Inertial focusing in 45° triangular channels with varying *Re* with $k = 0.24$ and $k = 0.45$. (a) and (b) The statistics of the particle positions (n = 1000) measured from the top view and side view. (c) and (d) The changes in inertial focusing positions with varying *Re* obtained from (a) and (b) and high-speed capture images of the corresponding peak positions. (e) The numerical simulations of the lift forces in half of the channel cross section for the condition $k = 0.45$ with varying *Re*.

pairwise inter-particle interaction, which would be an interesting topic to study in the future.

Numerical simulation of the lift force was conducted for half of the whole cross section [Fig. 3(e)], considering the mirror symmetry of an isosceles triangle. First, we checked the *Re* dependency when $k = 0.45$. The simulation results and the experimental results mostly agreed well but showed a slight yet noteworthy discrepancy. First, top corner focusing was found in the simulation results. The basin of attraction corresponding to this position was relatively small and becomes narrower as *Re* increases. This focusing position was not observed in the experiments, presumably due to how small the basins of attraction are. In addition, the top corner focusing position disappeared when $Re \geq 150$. No stable focusing position was found near the top corner. Second, the bottom face focusing position appeared when $Re \geq 150$, which was a higher *Re* than was observed in the experimental results. The bottom face focusing position first appeared as clouds of focusing positions and then merged into a single stable focusing position. The area of the basin of attraction increased with increasing *Re*, indicating the possibility of finding a particle was larger at this focusing position. Last, for the shift in the top face focusing, the simulation results suggest that it started first with a transition from bottom corner focusing to top face focusing. The focusing position near the bottom corner continuously shifts up until it nearly reaches the center of the sidewall face. This trend is very similar to the splitting and shift of the top focusing position that is found in 90° triangular channels.[32] Here, the symmetry is broken for the bottom corner, and the shift of the focusing position is along the long sidewall only. The shift of the focusing position along the bottom wall is suppressed, therefore, no apparent splitting is observed. The basin of attraction associated with the focusing position barely changes while the focusing position is shifting. In the experimental results, the focusing position from the side view shifted from $z/h = 0.27$–0.34. The focusing position in the simulation changed in the range of $z/h = 0.20$–0.34. While the exact values do not match between experiments and simulations, the trend is precisely captured.

The inertial focusing positions of the two different *k* values ($k = 0.24$ and 0.45) showed large differences at small *Re* in Fig. 3. We further investigated the details of the transition from small *k* to large *k* when $Re = 20$ (Fig. 4). Three face focusing positions (two top and one bottom) were observed in the experimental data when $k \leq 0.3$ [Fig. 4(a)]. The peaks corresponding to the bottom face focusing position ($y/w \sim 0$) were very broad in the top view; however, they can be clearly observed in the side view. These results agree with the simulation results. In case of small *k*, the bottom face focusing positions appear as a cloud of focusing positions along the bottom face. The simulation results show that the basin of attraction for the bottom face focusing became smaller with increasing *k* and disappeared when $k = 0.35$. The experimental results show a similar trend; the peak for the bottom focusing became noticeably smaller at $k = 0.38$ and disappeared at $k = 0.45$ in the side view. The *k* value at which the bottom face focusing position disappears does not exactly match in the experimental results and the simulation results. However, both results clearly show that the bottom face focusing position is stable at small *k* and becomes destabilized with increasing *k*.

No top corner focusing position was observed in the experiments with large *k*. However, the simulation results show that top corner focusing appeared when $k \geq 0.4$. Again, we think the small size of the corresponding basin of attraction makes it difficult to observe in the experiments. The top face focusing position shift observed in the experimental results was not only associated with changes in *Re* but also with changes in *k*. The top face focusing position shifted toward the bottom corner with increasing *k*. The focusing positions are found near the bottom corner at $k \geq 0.4$.

Inertial focusing in 120° triangular channels

Inertial focusing was studied previously in a right triangular channel.[16,32] Here, we investigated inertial focusing in an obtuse triangular channel with a wider apex angle of 120°. The trends of the inertial focusing position changes, such as top focusing position shifting and splitting, were almost identical to the trend found in 90° triangular channels. However, we found additional bottom focusing splitting in a 120° triangular channel when *k* was small and *Re* was high. Figure 5 shows the experimental and simulation data of inertial focusing with $k = 0.18$ and $(a, w, h) = (15\,\mu\text{m}, 304\,\mu\text{m}, 88\,\mu\text{m})$. Data for $k = 0.25$ and $(a, w, h) = (20\,\mu\text{m}, 304\,\mu\text{m}, 88\,\mu\text{m})$ are shown in Fig. S7 in the supplementary material for comparison. Experimental data for the top focusing positions and bottom focusing positions were analyzed separately [Figs. 5(a) and 5(b) and Fig. S7 in the supplementary material]. The particle distributions are broad compared to other triangular channel cases, and the bin size was chosen to be $5\,\mu\text{m}$. The locations of the particles on the different z axis could be easily distinguished by contrast in the high-speed images of the particles [Fig. 5(b)]. We intentionally adjusted the focus of the microscope near the top focusing positions, and the particles near the bottom of the channel went out-of-focus, resulting in blurry and darker images.

We first observed the distributions of particles near the top focusing positions for $k = 0.18$ [Figs. 5(a) and 5(b), left]. Two peaks were observed and the distance between the peaks became larger with increasing *Re*. When the particle size is relatively large ($k = 0.25$), we found one peak at low *Re*, which splits into two peaks (Fig. S7a in the supplementary material). Top corner focusing is split into two face focusing, and face focusing positions shift toward the side vertices of the triangle with increasing *Re* or decreasing *a*/*H*. This focusing position splitting and shifting trend is the same as the one observed in the 90° triangular channels.

Unexpected splitting of the bottom focusing position was observed with the increase of *Re* [Figs. 5(a) and 5(b), right]; the single peak became three peaks at $Re = 80$. The distance between the peaks became larger with increasing *Re*, showing a focusing position shift. The total number of focusing positions increased from three to five with increasing *Re* at $k = 0.18$. The focusing positions in the cross section were confirmed from confocal microscopy images [Fig. 5(c)]. Three focusing positions at $Re = 36$ become five positions at $Re = 107$, and the distance between the top focusing positions became larger at higher *Re*.

The simulation results show that the top corner focusing position splits become two face focusing positions with increasing *Re*. The focusing positions appeared as clouds of stable focusing

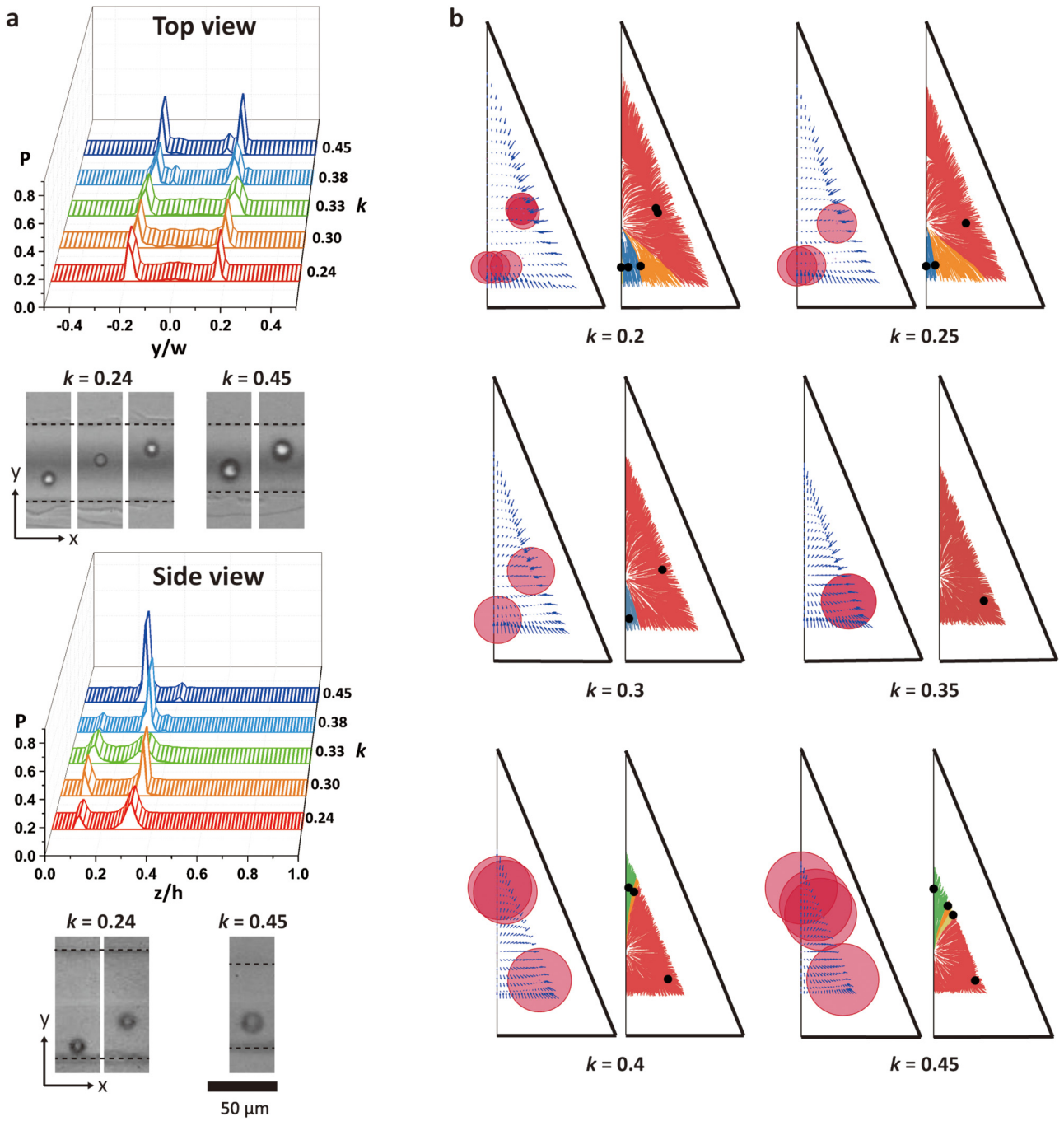

FIG. 4. Inertial focusing in 45° triangular channels with varying k at fixed Re ($Re = 20$). (a) The statistics of the particle positions measured from the top view and side view (n = 1000). (b) The numerical simulations of the lift forces in half of the channel cross section.

positions with further increase of Re, and they were included in several basins of attraction at $Re = 200$ [Fig. 5(d)]. A cloud of stable points makes sense because the particle distribution is quite broad, even though the bin size was $5\,\mu$m in the statistical distribution. Although additional clouds of focusing positions at the bottom corner were not observed in the experimental data, this could be explained by the small basins of attraction for the bottom corner focusing positions.

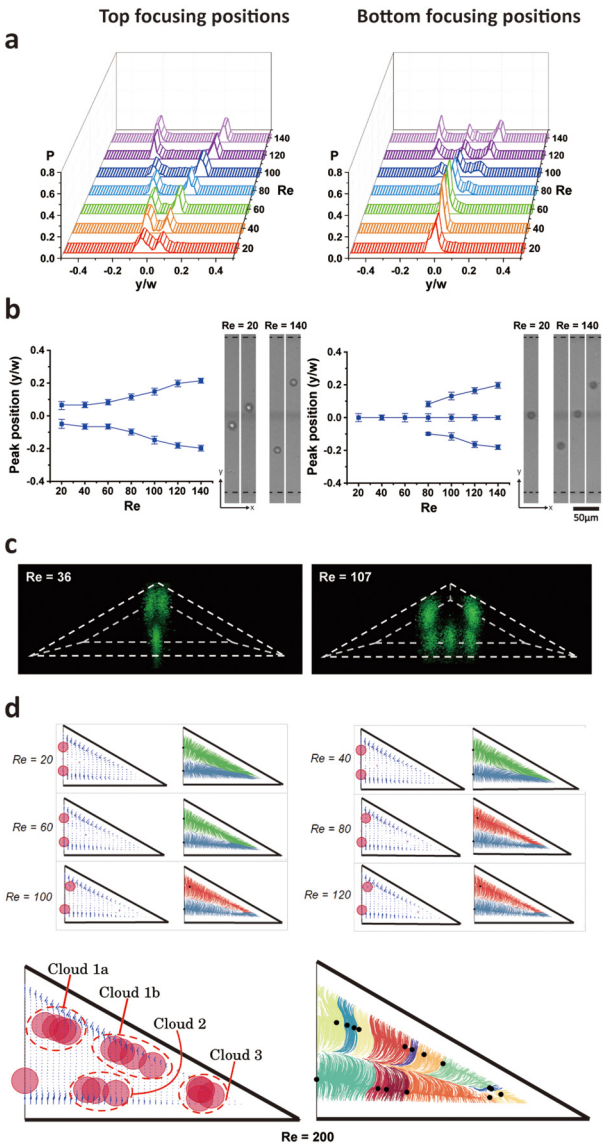

FIG. 5. Inertial focusing in 120° triangular channel with varying *Re* at $k = 0.18$. (a) The statistics of the particle positions measured from the top view. Particle positions near the top and bottom focusing positions were collected separately (n = 300). (b) The changes in inertial focusing positions with varying *Re* obtained from (a) and high-speed capture images of the corresponding peak positions. (c) Confocal microscopy images showing representative particle focusing positions of 3 and 5 focusing positions with $Re = 36$ and $Re = 107$ for $k = 0.18$. (d) The numerical simulations of the lift forces and inertial focusing positions in half of the channel cross section with varying *Re*.

DISCUSSION

The numerical and experimental results show that the triangular channels exhibited interesting dependence on *k*, *Re*, and the apex angle, which can allow precise control of the inertial focusing positions. Figure 6 summarizes the results of the changes in inertial focusing positions when *k* and *Re* were varied in 45°, 60°, 90°, and 120° triangular channels. We observed that the inertial focusing positions shifted as *Re* increased at fixed *k*, and the focusing pattern dramatically changed with different *k*. These focusing position shifts and focusing pattern changes were found to be strongly dependent on apex angles, as expected.

The top focusing positions generally shifted as *Re* increased with fixed *k*. The 60° triangular channel did not exhibit focusing position shift as expected. In the 45° triangular channel, the top focusing positions shifted with increasing *Re*, and the bottom focusing position stabilized and became observable experimentally at large *Re* (>100). The shifting direction was perpendicular to and away from the bottom wall. In the 120° triangular channel, the top corner focusing position split, and the resulting points shifted with increasing *Re*. The shifting direction was opposite to the 45° triangular channels; the focusing position shifted along the sidewalls and away from the apex.

The shifting of focusing positions along the channel face is a unique feature of inertial focusing in the triangular channels. Generally, inertial focusing of particles into equilibrium positions occurs in two stages: (1) fast migration toward channel faces due to the strong shear-gradient lift force and (2) slow migration toward the center of the channel faces by the wall-effect lift forces parallel to the channel faces. As an example, in a low-aspect-ratio rectangular channel, the wall-effect lift forces arising from the vertical sidewalls are symmetric and equilibrate at the centers of the horizontal channel faces. Therefore, the change of focusing positions with varying *Re* is limited to a small amount in the direction of shear gradient, or toward the channel face, due to the different scaling of the shear-gradient lift force and wall-effect lift force to *Re*. However, the symmetry of the wall-effect lift force toward the center of the channel faces is broken for top focusing positions in triangular channels. Along the sidewalls, the wall-effect lift force from the other sidewall and bottom wall is the dominant force that determines the location of the focusing position. As we explained in the previous study,[16,32] the scaling of the wall-effect lift force with *Re* is a function of the distance from the channel wall; the wall-effect lift force increases faster in the vicinity of the channel walls. Therefore, the direction of the focusing position shift is reversed in the 45° triangular channel compared to the 90° and 120° triangular channels.

In 120° triangular channels, additional splitting and shifting of the bottom focusing position were observed. A similar phenomenon was observed in a rectangular channel; at $Re > 100$, the focusing positions near the centers of the long channel faces can split and shift toward the short channel face.[19] This can be attributed to splitting by the forces arising from the induced pressure difference, known as the "Bernoulli-like effect." The bottom focusing position of the 120° triangular channels can be explained in the same way because the flow velocity profile has a large similarity to the focusing positions in a low-aspect-ratio rectangular channel.

The focusing pattern was found to show dramatic changes depending on *k*. Relatively large particles are focused at the corner focusing positions when the vertex angle is larger than, or equal to, 60°. The corner focusing position is an unusual focusing position that is rarely observed in inertial microfluidics. The possible existence of corner focusing was only suggested by numerical data in square channels. Chun and Ladd[43] predicted that corner focusing

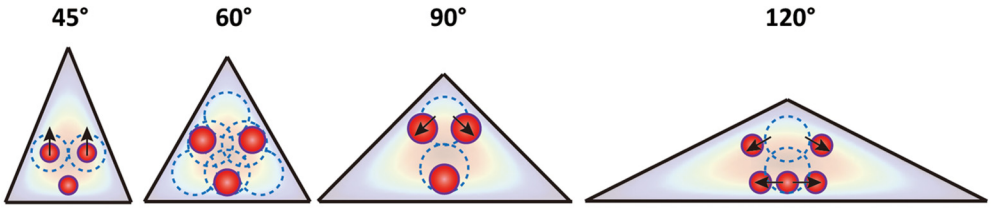

FIG. 6. The changes in the inertial focusing positions with *k* and *Re* in triangular channels with various apex angles. Black arrows indicate the direction of focusing position shift with increasing *Re*. For a large *k* value (blue dotted circle), corner focusing was observed for large *Re* range. The schematic for 90° triangular channel is based on the previous research (Ref. 32).

would be observed at high *Re* ($Re > 100$), and Prohm and Stark[18] predicted that corner focusing exists at high *k* and low *Re*. However, no corner focusing was observed up to very high *Re*.[14] Like this case, corner focusing positions were observed as stable equilibrium near all vertices, in addition to face focusing positions when *k* was large and *Re* was low. With decreasing *k* or increasing *Re*, the basins of attraction corresponding to corner focusing became narrow, and face focusing positions became dominant. We concluded that corner focusing can be formed near a vertex that is larger than or equal to 60°, and the range of conditions for corner focusing becomes wider as the angle increases. Accordingly, the corner focusing position can be observed near the apex in 90° and 120° triangular channels and is maintained within the specific range depending on the angle. This finding of corner focusing provides the clue to the mechanism of the splitting and the shifting of the focusing positions in addition to the different scaling of the wall-effect lift force and shear-gradient lift force with respect to *Re*. Previously, the top corner focusing in a right triangular channel was understood based on the similarity of the velocity profile within a half circular channel or a low-aspect-ratio rectangular channel. The experimental and simulation results in this study show that the corner focusing position is a stable equilibrium position that can be generally found at low *Re* conditions. As a consequence, the splitting and shifting of the focusing position can be understood as competition and transition of the dominant focusing mode from corner focusing to face focusing.

The 45° triangular channel showed an inertial focusing tendency similar to that of the high-aspect-ratio rectangular channel. Particles were focused at two focusing positions near each sidewall, and an additional bottom face focusing position was stabilized with increasing *Re* at fixed *k* or decreasing *k* with fixed *Re*. This was also observed in the rectangular channel; unstable focusing positions near the short channel walls became stabilized as *Re* increased or *k* decreased.[1,19] This occurs because the increase in shear-gradient lift force is relatively larger than the increase in wall-effect lift forces along the centerline of the cross section.

CONCLUSION

We investigated inertial focusing in triangular channels with various vertex angles (45°, 90°, 60°, and 120°). We mainly observed the shifting of focusing positions with increasing *Re* at fixed *k*. The focusing patterns were dependent on *k*. When the apex angle was larger than or equal to 60°, corner focusing, in particular, was observed, both experimentally and numerically. Equilateral triangular channels did not exhibit large changes except for a small range of conditions. When *k* was large and *Re* was low, additional corner focusing positions were formed near all corners. In the 90° and 120° triangular channels, the top focusing position splitted and shifted along the sidewalls with increasing *Re*. The onset *Re* that splitted the top focusing position was higher for a larger *k*. In addition, a 120° triangular channel showed splitting and shifting of the bottom focusing positions toward the vertices on each side. The transition of dominant focusing mode from the corner focusing at low *Re* to face focusing at high *Re* provides a mechanistic explanation of the top focusing position splitting and shifting.

In the 45° triangular channel, two top face focusing positions became three face focusing positions with a new focusing position appearing near the bottom wall (short face). The trend was similar to that of a high-aspect-ratio rectangular channel. In addition, the top focusing positions shifted toward the apex, which was the opposite direction of the 90° and 120° triangular channels. The changes in the focusing pattern and the focusing position shift were found to depend on the angles. Therefore, adjusting the angles was determined to be a method for controlling the direction and strength of lift forces. This suggests that the roles of shear-gradient lift force and wall-effect lift force can be separately understood. In addition, various focusing patterns provide new guidelines for device designs for various applications. As new fabrication methods enhance our ability to make arbitrary cross-sectional shapes, a deeper understanding of cross section dependent inertial focusing will become important.

SUPPLEMENTARY MATERIAL

See the supplementary material for the following topics. Planing process (Fig. S1). Conditions for experimental and numerical investigations (Table S1). Definitions of various parameters and observation directions (Fig. S2). Confocal microscopy images of inertial focusing configuration changes for small and large *k* values (Fig. S3). Naming of the focusing positions (Fig. S4). The statistics of the particle position measured from the side view for the condition $k = 0.45$ at $Re = 60$, 80, and 100 (Fig. S5). The comparison of original data and pair-particle elimination at $k = 0.45$ and $Re = 20$ in 45° triangular channel (Fig. S6). The statistics of the particle positions measured from the top view at $k = 0.25$ in 120° triangular channels (Fig. S7).

AUTHORS' CONTRIBUTIONS

J.K. and A.K. contributed equally to this work.

ACKNOWLEDGMENTS

This research was supported by the KAISTGrand Challenge 30 Project funded by KAIST and the Ministry of Science and ICT, Korea (1711100591/N11190158) and the Basic Research Program in Science and Engineering funded by the National Research Foundation (NRF-2018R1A2B6003793).

REFERENCES

[1]H. Amini, W. Lee, and D. Di Carlo, Lab Chip **14**(15), 2739–2761 (2014).
[2]D. Di Carlo, Lab Chip **9**(21), 3038–3046 (2009).
[3]J. M. Martel and M. Toner, Annu. Rev. Biomed. Eng. **16**, 371–396 (2014).
[4]J. Zhang, S. Yan, D. Yuan, G. Alici, N.-T. Nguyen, M. Ebrahimi Warkiani, and W. Li, Lab Chip **16**(1), 10–34 (2016).
[5]D. Stoecklein and D. Di Carlo, Anal. Chem. **91**(1), 296–314 (2019).
[6]A. J. Chung, BioChip J. **13**(1), 53–63 (2019).
[7]G. SegrÉ and A. Silberberg, Nature **189**(4760), 209–210 (1961).
[8]E. S. Asmolov, J. Fluid Mech. **381**, 63–87 (1999).
[9]D. Di Carlo, J. F. Edd, K. J. Humphry, H. A. Stone, and M. Toner, Phys. Rev. Lett. **102**(9), 094503 (2009).
[10]D. R. Gossett, W. M. Weaver, A. J. Mach, S. C. Hur, H. T. K. Tse, W. Lee, H. Amini, and D. Di Carlo, Anal. Bioanal. Chem. **397**(8), 3249–3267 (2010).
[11]P. Sajeesh and A. K. Sen, Microfluid. Nanofluid. **17**(1), 1–52 (2014).
[12]M. E. Piyasena and S. W. Graves, Lab Chip **14**(6), 1044–1059 (2014).
[13]G.-Y. Kim, J.-I. Han, and J.-K. Park, BioChip J. **12**(4), 257–267 (2018).
[14]A. T. Ciftlik, M. Ettori, and M. A. M. Gijs, Small **9**(16), 2764–2773 (2013).
[15]S. C. Hur, S.-E. Choi, S. Kwon, and D. D. Carlo, Appl. Phys. Lett. **99**(4), 044101 (2011).
[16]J. Kim, J. Lee, C. Wu, S. Nam, D. Di Carlo, and W. Lee, Lab Chip **16**(6), 992–1001 (2016).
[17]D. R. Gossett, H. T. K. Tse, J. S. Dudani, K. Goda, T. A. Woods, S. W. Graves, and D. Di Carlo, Small **8**(17), 2757–2764 (2012).
[18]C. Prohm and H. Stark, Lab Chip **14**(12), 2115–2123 (2014).
[19]C. Liu, G. Hu, X. Jiang, and J. Sun, Lab Chip **15**(4), 1168–1177 (2015).
[20]J. Zhou, P. V. Giridhar, S. Kasper, and I. Papautsky, Lab Chip **13**(10), 1919–1929 (2013).
[21]A. P. Tan, J. S. Dudani, A. Arshi, R. J. Lee, H. T. K. Tse, D. R. Gossett, and D. Di Carlo, Lab Chip **14**(3), 522–531 (2014).
[22]S. S. Kuntaegowdanahalli, A. A. S. Bhagat, G. Kumar, and I. Papautsky, Lab Chip **9**(20), 2973–2980 (2009).
[23]J. Zhang, W. Li, M. Li, G. Alici, and N.-T. Nguyen, Microfluid. Nanofluid. **17**(2), 305–316 (2014).
[24]E. Sollier, D. E. Go, J. Che, D. R. Gossett, S. O'Byrne, W. M. Weaver, N. Kummer, M. Rettig, J. Goldman, N. Nickols, S. McCloskey, R. P. Kulkarni, and D. Di Carlo, Lab Chip **14**(1), 63–77 (2014).
[25]D. Yuan, Q. Zhao, S. Yan, S.-Y. Tang, G. Alici, J. Zhang, and W. Li, Lab Chip **18**(4), 551–567 (2018).
[26]J. D. Adams and H. T. Soh, Appl. Phys. Lett. **97**(6), 064103 (2010).
[27]A. Munaz, M. J. A. Shiddiky, and N.-T. Nguyen, Biomicrofluidics **12**(3), 031501–031501 (2018).
[28]G. Holzner, S. Stavrakis, and A. deMello, Anal. Chem. **89**(21), 11653–11663 (2017).
[29]Y. Liu, A. Hansen, E. Block, N. R. Morrow, J. Squier, and J. Oakey, J. Colloid Interface Sci. **507**, 234–241 (2017).
[30]R. Yuan, J. Lee, H.-W. Su, E. Levy, T. Khudiyev, J. Voldman, and Y. Fink, Proc. Natl. Acad. Sci. U.S.A. **115**(46), E10830–E10838 (2018).
[31]W. Tang, N. Fan, J. Yang, Z. Li, L. Zhu, D. Jiang, J. Shi, and N. Xiang, Microfluid. Nanofluid. **23**(3), 42 (2019).
[32]J.-A. Kim, J.-R. Lee, T.-J. Je, E.-C. Jeon, and W. Lee, Anal. Chem. **90**(3), 1827–1835 (2018).
[33]P. Mukherjee, X. Wang, J. Zhou, and I. Papautsky, Lab Chip **19**(1), 147–157 (2019).
[34]Z. Chen, L. Zhao, L. Wei, Z. Huang, P. Yin, X. Huang, H. Shi, B. Hu, and J. Tian, Sens. Actuators B **301**, 127125 (2019).
[35]S. Darvishi, T. Cubaud, and J. P. Longtin, Opt. Lasers Eng. **50**(2), 210–214 (2012).
[36]S. M. Nam, K. Kim, I.-S. Kang, W. Park, and W. Lee, BioChip J. **13**(3), 226–235 (2019).
[37]A. E. Reece and J. Oakey, Phys. Fluids **28**(4), 043303 (2016).
[38]K. J. Humphry, P. M. Kulkarni, D. A. Weitz, J. F. Morris, and H. A. Stone, Phys. Fluids **22**(8), 081703 (2010).
[39]J. Zhou and I. Papautsky, Lab Chip **13**(6), 1121–1132 (2013).
[40]A. Kommajosula, J.-A. Kim, W. Lee, and B. Ganapathysubramanian arXiv:1901.05561 (2019).
[41]T. E. Tezduyar, S. Mittal, S. E. Ray, and R. Shih, Comput. Method. Appl. Mech. Eng. **95**(2), 221–242 (1992).
[42]W. Lee, H. Amini, H. A. Stone, and D. Di Carlo, Proc. Natl. Acad. Sci. U.S.A. **107**(52), 22413–22418 (2010).
[43]B. Chun and A. J. C. Ladd, Phys. Fluids **18**(3), 031704 (2006).